Fast Charge Sensing of a Cavity-Coupled Double Quantum Dot Using a Josephson Parametric Amplifier

J. Stehlik,[1] Y.-Y. Liu,[1] C. M. Quintana,[1,2] C. Eichler,[1] T. R. Hartke,[1] and J. R. Petta[1,2]
[1]*Department of Physics, Princeton University, Princeton, New Jersey 08544, USA*
[2]*Department of Physics, University of California, Santa Barbara, California 93106, USA*
(Received 4 February 2015; revised manuscript received 15 May 2015; published 27 July 2015)

We demonstrate fast readout of a double quantum dot (DQD) that is coupled to a superconducting resonator. Utilizing a parametric amplifier beyond its range of linear amplification, we improve the signal-to-noise ratio (SNR) by a factor of 2000 compared to the situation with the parametric amplifier turned off. With an integration time of 400 ns comparable to the inverse effective bandwidth, we achieve a SNR of 76. By measuring the SNR as a function of the integration time, we extract an equivalent charge sensitivity of $8 \times 10^{-5}\ e/\sqrt{\mathrm{Hz}}$. The high SNR allows us to acquire a DQD charge-stability diagram in just 20 ms. At such a high data rate, it is possible to acquire charge-stability diagrams in a live "video mode," enabling real-time tuning of the DQD confinement potential.

DOI: 10.1103/PhysRevApplied.4.014018

I. INTRODUCTION

Conventional charge transport experiments directly measure the electrical conductance or current flow through a sample. Instead of measuring the rate at which electrons flow through a sample, it is sometimes desirable to have direct access to the charge degree of freedom using sensitive electrometers. For example, charge sensing can be used for real-time counting of electrons [1], imaging of current flow through nanostructures such as quantum point contacts [2], imaging electron-hole puddles in graphene [3], and single-electron capacitance spectroscopy of quantum Hall states [4,5]. Charge detection is also a necessary ingredient for quantum computation using electrons trapped in gate-defined quantum dots [6,7]. For spin qubits, a process called spin-to-charge conversion is used for readout [8,9]. Charge sensing is also needed to accurately measure the charge-stability diagram of double quantum dots (DQDs) and determine the absolute electron occupancy. Sensing in quantum dots has traditionally been performed using quantum point contacts (QPCs) or single-electron transistors (SETs) [10–12].

One method to improve the charge-sensing bandwidth involves embedding the QPC or SET in a resonant tank circuit and performing rf reflectometry [13–15]. Reflectometry experiments have so far utilized standard cryogenic low-noise amplifiers [16]. The increased data acquisition rate of rf-based measurements reduces the susceptibility to $1/f$ noise and enables single-shot spin readout [17].

While rf reflectometry has allowed charge detection times as short as 100 ns with a signal-to-noise ratio (SNR) of approximately 10 [18,19], embedding a rf-QPC or rf-SET in a quantum device is not always feasible or desirable. An alternative route towards significant SNR improvements is offered by the application of Josephson parametric amplifiers (JPAs), which have recently accelerated progress in the field of superconducting circuits [20–26]. JPAs are quantum limited in the sense that the dominant amount of their added noise originates from vacuum fluctuations [22,27,28]. They have enabled high-fidelity single-shot readout of qubit states [29,30], realization of quantum feedback protocols [31,32], precise readout of nanomechanical resonators [33], exploration of higher-order photon field correlations [34], as well as squeezed light experiments [22,35,36].

In this paper, we demonstrate JPA-assisted readout of a DQD that is coupled to a high-frequency superconducting cavity. We achieve a factor of 2000 improvement in the SNR using a readout signal that exceeds the dynamic range of the JPA. Here the signal experiences a larger amplification than the incoming noise. The large SNR allows us to efficiently map out the DQD charge-stability diagram in just 20 ms using a dual gate-voltage rastering scheme. Such dramatic improvements enable real-time "video-mode" tuning of a DQD device. The improvements in sensitivity that JPA-assisted readout provides can be utilized to more efficiently optimize the increasingly complex quantum-dot architectures that are being developed [37–39].

II. EXPERIMENTAL SETUP

The mechanism employed for the readout of the charge states of the DQD is based on the electrical dipole coupling between the DQD and the superconducting microwave cavity. Because of this coupling, the DQD imposes a frequency shift and an additional load onto the cavity, which depends on the DQD's internal state [40–42]. We probe this induced change of the cavity transmission

coefficient with a coherent tone applied to the cavity at frequency $f_{\rm in} = 7881$ MHz and power $P_{\rm in} = -110$ dBm. The readout of the DQD charge states, thus, translates into discriminating between microwave fields of different amplitude and phase. We improve the SNR of this discrimination by utilizing a JPA. The device used for our experiment consists of two InAs DQDs of which one is left idle throughout the experiment. The device architecture and readout chain (see Fig. 1) are described in detail below.

The DQD is fabricated using a bottom-gated architecture as shown in Fig. 1(b) [43]. We place a single InAs nanowire of nominally 50 nm diameter [44] across five depletion gates [45]. We label the gates $V_{\rm LW}$, $V_{\rm L}$, $V_{\rm M}$, $V_{\rm R}$, and $V_{\rm RW}$. A double-well potential is formed by selectively depleting

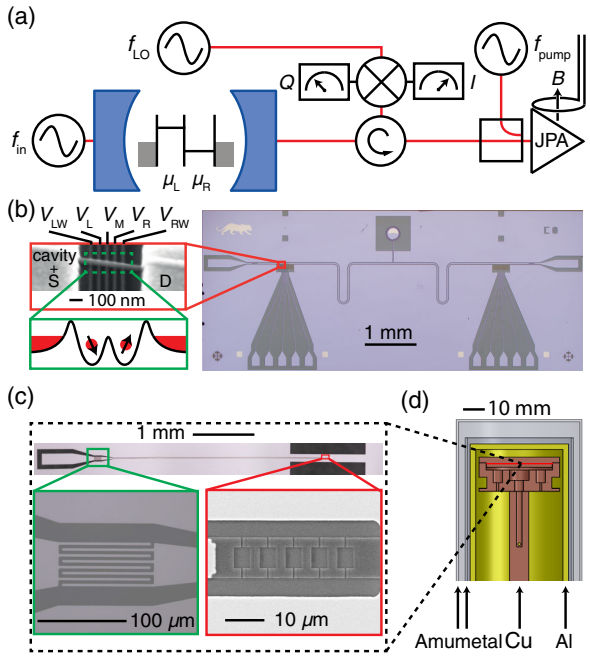

FIG. 1. (a) Diagram of the experimental setup. A readout tone at frequency $f_{\rm in}$ is applied to the cavity input port. The output field of the cavity is sent through a circulator, amplified using a JPA, and then demodulated into the I and Q quadratures. The amplification band of the JPA is flux tuned using a small coil that creates a magnetic field B. A directional coupler is used to couple in the pump field at frequency $f_{\rm pump}$. (b) Illustration of the DQD cavity system. A single nanowire is placed on top of five depletion gates. Negative voltages on the gates establish a double-well potential forming the DQD. (c) Optical micrograph of the JPA, which is implemented as a quarter-wavelength resonator shunted by an array of five SQUIDs. The resonator is coupled to the input port using an interdigitated planar capacitor (outlined in green). A scanning electron micrograph showing the SQUID array is outlined in red. (d) Schematic of the magnetic shielding used to isolate the JPA from the superconducting magnet around the DQD. The JPA is housed in a copper box magnetically shielded by one aluminum and two Amumetal 4K cylinders.

the nanowire using the bottom gates [45]. Here, $V_{\rm LW}$ and $V_{\rm RW}$ control the left and right barriers, $V_{\rm L}$ and $V_{\rm R}$ control $\mu_{\rm L}$ and $\mu_{\rm R}$, the electrochemical potential of each dot, and $V_{\rm M}$ controls the interdot tunneling rate [7]. After passivating the nanowire using an ammonium polysulfide etch [46], we deposit Ti/Au contacts to form the source and drain electrodes.

The source contact of the DQD is connected to a voltage antinode of a half-wavelength superconducting resonator with a resonance frequency $f_c = 7881$ MHz; see Fig. 1(b) [41]. The drain is connected to the resonator ground plane. The resonator is fabricated from a 50-nm-thick Nb film, which is sputter deposited on a high-resistivity silicon substrate with a 250-nm-thick layer of thermally grown SiO_2. The input and output capacitors result in input and output coupling rates $\kappa_{\rm in}/2\pi \approx \kappa_{\rm out}/2\pi \approx 0.39$ MHz. Additional internal radiation losses result in a total cavity decay rate $\kappa_{\rm tot}/2\pi = 2.6$ MHz equivalent to a loaded quality factor $Q_c \sim 3000$.

As shown in Fig. 1(c), the JPA is implemented as a quarter-wavelength resonator etched from a 200-nm Nb layer on top of a sapphire substrate [22,36]. The input port has a coupling rate $\kappa_{\rm JPA}/2\pi \approx 100$ MHz and is formed using an interdigitated capacitor geometry with a capacitance of approximately 40 fF. The resonator is shunted by a series array of $M = 5$ superconducting quantum interference devices (SQUIDs), which are fabricated from aluminum using the Dolan bridge technique [47]. The SQUIDs act as a nonlinear inductive element required for amplification. Using an array of $M = 5$ SQUIDs enhances the dynamic range compared to single SQUID designs [48]. We design each SQUID to have a maximal Josephson energy $E_J/h = 7 \pm 0.5$ THz corresponding to a critical current $I_c = 14$ μA. A detailed treatment of the design considerations of this class of amplifiers is given in Ref. [48].

The JPA is protected by three layers of magnetic shielding [see Fig. 1(d)] to allow for operation in the presence of a large external magnetic field, as required for spin qubit experiments. Two concentric Amumetal 4K cylinders provide a high degree of isolation from the magnetic field that is generated by the superconducting magnet. The third inner cylinder is made of superconducting aluminum and shields the JPA due to the Meissner effect. For magnetic fields up to 100 mT, we detect no shift in the JPA resonance frequency.

III. OPERATIONAL MODE OF THE JOSEPHSON PARAMETRIC AMPLIFIER

We characterize the JPA resonance in the linear regime by measuring the reflected phase Φ as a function of current through a bias coil mounted below the JPA. The applied magnetic field changes the flux threaded through the SQUID loops, which modulates the effective Josephson inductance and with it the resonance frequency;

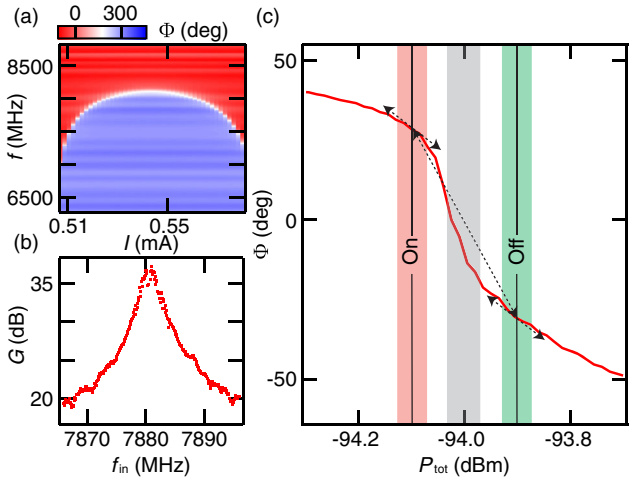

FIG. 2. (a) Reflected phase Φ as a function of bias coil current I and probe frequency f. The resonance frequency of the JPA is indicated by a large phase shift. (b) Gain as a function of frequency for the JPA configured as a linear amplifier in phase-insensitive mode. We achieve a gain of approximately 4000 (36 dB) with a bandwidth $B_w = 3.8$ MHz. (c) Phase Φ of the signal reflected off of the JPA as a function of the total incident power P_{tot}. Grey area indicates the power range around $P_{\mathrm{pump}} = -94$ dBm for which amplification is approximately linear. Green- and red-shaded areas schematically represent noise-induced power fluctuations around the average P_{tot} associated with the DQD on and off state, respectively.

see Fig. 2(a). In order to operate the device as an amplifier, we make use of the nonlinear nature of the JPA resonance. By pumping it with a strong coherent tone at frequency $f_{\mathrm{pump}} = f_c$ and power $P_{\mathrm{pump}} = -94$ dBm, we achieve wave mixing processes leading to parametric gain. We characterize the band of amplification by applying a weak test tone at frequency f and measuring the power gain G. For the chosen pump configuration, the resulting gain exceeds 30 dB with a nearly Lorentzian-shaped gain profile of width $B_w = 3.8$ MHz as shown in Fig. 2(b).

For the purpose of this experiment, we utilize the amplifier in phase-sensitive mode by setting the frequency of the cavity probe f_{in} equal to the pump frequency f_{pump} [22,49]. In this operational mode, the origin of amplification can be understood from the power-dependent phase response of the JPA; see Fig. 2(c). The signal to be amplified changes the total power P_{tot} incident on the JPA, resulting in a large measurable phase shift. The pump power of $P_{\mathrm{pump}} = -94$ dBm is chosen to maximize the slope $|d\Phi/dP_{\mathrm{tot}}| \approx 600°/\mathrm{dBm}$. The total power P_{tot} depends on the amplitude and phase of the cavity output field according to

$$P_{\mathrm{tot}} = |\sqrt{P_{\mathrm{pump}}} + t\sqrt{P_{\mathrm{in}}}e^{i\phi_r}|^2. \quad (1)$$

Here, t is the complex cavity transmission coefficient, and ϕ_r is the relative phase shift between the cavity input and pump fields. For cavity output powers $|t|^2 P_{\mathrm{in}} \lesssim -135$ dBm, this change in power is small such that the phase gradient $d\Phi/\mathrm{d}P_{\mathrm{tot}}$ is approximately constant [gray-shaded area in Fig. 2(c)] and the JPA behaves like a linear amplifier.

In contrast, here we operate the amplifier beyond its range of linear amplification by increasing the cavity probe power to $P_{\mathrm{in}} = -110$ dBm. This introduces amplitude-dependent amplification leading to further improvements in the SNR when discriminating between the two relevant charge states of the DQD. We label these states as "on" and "off" for convenience. For the chosen readout and pump power configuration, we estimate P_{tot} to be −94.1 dBm for the on state and −93.9 dBm for the off state, as indicated in Fig. 2(c). Around both the on and off state, $|d\Phi/dP_{\mathrm{tot}}| \lesssim 100°/\mathrm{dBm}$, which is significantly smaller than the average $|d\Phi/dP_{\mathrm{tot}}| \approx 300°/\mathrm{dBm}$ between the two states. As a result, the average signal associated with the difference between the on and off states is amplified more than the small fluctuations around the two states. Operation in the nonlinear amplification regime can, thus, improve the SNR beyond the limits imposed on linear amplifiers [27].

The signal exiting the JPA is further amplified using a high-electron-mobility transistor (HEMT) amplifier at the 3-K stage of the dilution refrigerator and room-temperature amplifiers (see Appendix A for a complete circuit diagram). We can turn off the JPA by simply removing the pump tone. Here the signal from the cavity reflects off of the JPA with unity gain. In both cases, we demodulate the signal using a heterodyne detection setup. We first down convert the signal to 12.5 MHz by mixing it with a local oscillator tone $f_{\mathrm{LO}} = f_{\mathrm{in}} + 12.5$ MHz. It is then digitized using a FPGA-based digital homodyne stage to recover the I and Q quadrature amplitudes.

IV. DOUBLE-QUANTUM-DOT CHARGE DETECTION

We now highlight the dramatic enhancement in the data acquisition rate that is enabled by the JPA. We first demonstrate rapid measurements of a large-scale DQD charge-stability diagram. We then compare the SNR values obtained with and without the JPA. Finally, we demonstrate video-mode acquisition of charge-stability diagrams using a rastered sweep of two gate voltages. The resulting data display is similar to a cathode ray tube and of a comparable refresh rate.

A. Double-quantum-dot charge-stability diagram

A large-scale charge-stability diagram is shown in Fig. 3, where we plot the normalized Q quadrature amplitude as a function of V_{L} and V_{R}. These data are acquired by measuring the total reflected field from the JPA with the JPA pump tone on. With the DQD in Coulomb blockade, the resonator is insensitive to the DQD, resulting in large

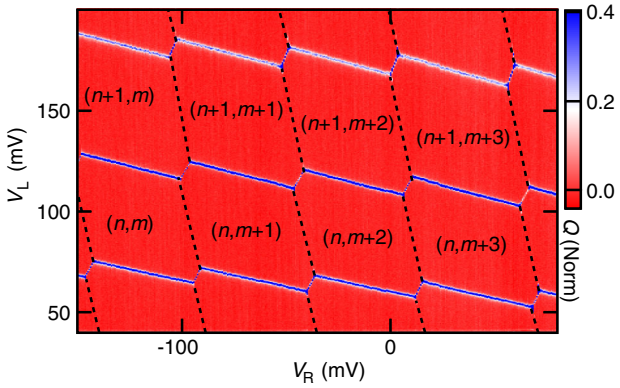

FIG. 3. DQD charge-stability diagram extracted by plotting the normalized Q quadrature amplitude as a function of gate voltages V_L and V_R. The plot is taken with the JPA turned on and takes only 2 min to acquire. Dashed lines are guides to the eye.

regions in the stability diagram with uniform amplitude and phase. Following previous work, we normalize the amplitude $A = I + iQ$, such that $|A| = 1$ and $\arg(A) = 0$ in these charge-stability islands [41]. With this normalization, the sensitivity of the Q quadrature to charge transitions is maximized, and its mean value in Coulomb blockade is $\langle Q \rangle = 0$.

When an electron can tunnel between the two dots (interdot charge transition) or on and off one of the dots (single-dot charge transition), the transmitted field through the resonator will be affected, which we detect as a nonzero Q quadrature amplitude. As a result, the data in Fig. 3 trace out the charge-stability diagram of the DQD [7]. The nearly horizontal lines are associated with the addition or removal of an electron from the left dot. The lines with positive slope correspond to interdot charge transitions where the total electron number is fixed, but an electron moves from one dot to the other. Because of the large distance between the cavity center pin and the right tunnel barrier, right-dot charge transitions are not visible. We can infer their location based on the positions of the interdot charging lines. We use the charging lines to label the electron states as (n, m), where n (m) is the number of electrons on the left (right) dot. For this data set, the device is configured in the many-electron regime, where $n \sim m \sim 20$. We note that the data shown in Fig. 3 are acquired in just 2 min. In comparison, acquiring similar quality data using our previous rf-reflectometry approach would take 20 min [50]. Measurements using standard low-frequency conductance measurements of a quantum point contact require approximately an hour.

B. Signal-to-noise measurements

To quantify the improvement in the SNR due to the JPA, we investigate the sensing signal at an interdot charge transition. Interdot charge transitions are most relevant in quantum control experiments since interdot tunneling is spin selective and can be used to distinguish spin singlet and triplet states [9,41,51,52]. Figures 4(a) and 4(b) show charge-stability diagrams obtained near the $(n, m+1) \leftrightarrow (n-1, m+2)$ interdot charge transition. For each point of the color map, the Q quadrature is averaged for $\tau = 42$ μs. For a direct comparison, the data in Fig. 4(a) are acquired with the JPA turned on, while the data in Fig. 4(b) are acquired with the JPA turned off. The dramatic increase in the visibility of the charge transitions in Fig. 4(a) provides direct confirmation of an increased SNR when the JPA is used. For a quantitative comparison, we ramp the gate voltage V_L along the dashed lines shown in Figs. 4(a) and 4(b) with a 50-Hz repetition rate and record time traces of the resultant Q quadrature amplitude. To study the SNR as a function of the effective per-point integration time τ, we oversample at 12.5×10^6 samples/s and then apply an

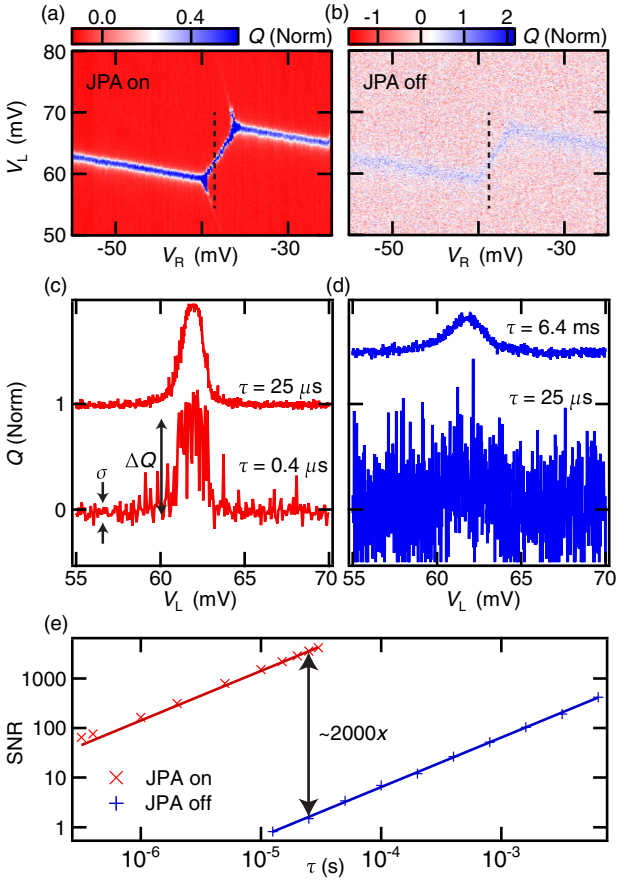

FIG. 4. (a),(b) Q quadrature amplitude plotted as a function of V_L and V_R near the $(n, m+1) \leftrightarrow (n-1, m+2)$ interdot charge transition. (a) Data taken with the JPA on, and (b) with the JPA off. For both cases, each point of the color map is integrated for $\tau = 42$ μs. (c),(d) Traces of the Q quadrature amplitude showing the interdot charge transition for different per-point integration times τ. (c) Data taken with the JPA on (traces are offset by 1 for clarity), and (d) with the JPA off (traces are offset by 1.5 for clarity). (e) SNR for the interdot charge transition as a function of the integration time τ. Amplification with the JPA results in a factor of 2000 improvement in the SNR. Solid lines are fits to Eq. (2).

appropriately sized digital box-car filter (see Appendix B). The results for $\tau = 400$ ns and $\tau = 25$ μs with the JPA turned on are shown in Fig. 4(c). Even with $\tau = 400$ ns, the interdot signal is clearly discernible. Following standard electronic references, we define the SNR as the ratio of the signal power to the noise power in the measured channel [53]. Using this definition,

$$\mathrm{SNR} = \frac{\Delta Q^2}{\sigma^2}, \tag{2}$$

where ΔQ is the amplitude of the interdot charge transition signal, and σ is the root-mean-square amplitude of the noise of the Q quadrature in Coulomb blockade [see Fig. 4(c)]. In the case of $\tau = 400$ ns, we obtain a SNR ≈ 76.

As illustrated by the data in Fig. 4(d), the SNR is much worse when only the HEMT is used. With $\tau = 25$ μs, the SNR $= 1.4$, meaning the interdot charge transition is barely resolvable. The signal can be recovered by increasing τ. Increasing τ beyond 500 μs is accomplished by averaging multiple time traces (see Appendix B). The result for $\tau = 6.4$ ms is shown in the upper trace of Fig. 4(d).

The SNR is plotted as a function of the effective integration time τ in Fig. 4(e) with the JPA on and off. In both cases, the curves are very well fit with

$$\mathrm{SNR}(\tau) = \frac{\tau}{\tau_{\mathrm{min}}}. \tag{3}$$

Here, τ_{min} is a fitting parameter that corresponds to the minimum integration time required to achieve a SNR $= 1$. With the JPA on, a best fit is obtained with $\tau_{\mathrm{min}}^{\mathrm{on}} = 7$ ns, while with the JPA off $\tau_{\mathrm{min}}^{\mathrm{off}} = 16$ μs, corresponding to a factor of 2000 improvement in the SNR. The linear dependence of the SNR on τ is expected and can be understood from the fact that τ sets the effective low-pass filter of the detection chain. Decreasing τ increases the bandwidth and, therefore, the noise power, while the signal power will remain constant [53].

We now estimate the minimum time required for single-charge detection in terms of both sensitivity and ultimate bandwidth. From the fitting described above, the minimum integration time necessary for a SNR $= 1$ is $\tau_{\mathrm{min}}^{\mathrm{on}} = 7$ ns. Since charge sensitivity is related to minimum integration time through $S = e\sqrt{\tau_{\mathrm{min}}}$, our detector has an equivalent charge sensitivity of 8×10^{-5} $e/\sqrt{\mathrm{Hz}}$ [17,19]. This charge sensitivity is about an order of magnitude below the sensitivities achieved in state-of-the-art rf-SETs [54] and 2 orders of magnitude above sensitivities obtained in comparable DQD setups [19].

The bandwidth of our detection chain is limited by the cavity linewidth and the JPA bandwidth. The former is set by $\kappa_{\mathrm{tot}}/2\pi \approx 2.6$ MHz and can be extended by increasing the output coupling capacitance. The latter is constrained by the JPA bandwidth. In our case, we estimate the JPA bandwidth to be approximately 3.8 MHz based on measurements in the linear regime. This limit can be circumvented by more advanced amplifier designs [55–58]. The above means that we are bandwidth limited by the cavity to detection times longer than approximately 400 ns.

C. Video-mode data acquisition

With the high SNR obtained at integration times as low as $\tau = 400$ ns, it is possible to acquire 100×100 point color maps in just 4 ms. We take advantage of the fast data acquisition by developing a dual gate-voltage rastering scheme illustrated in the lower inset of Fig. 5. Starting in the lower left corner of the charge-stability diagram, we repeatedly ramp V_{R} with a 40-μs period. At the same time, we also ramp V_{L} with a 20-ms period. The resulting data set rasters over a two-dimensional voltage subspace within a 20-ms period. During this time, we record a single time trace of the measured quadrature with $\tau = 400$ ns and reorder it to form a 2D image that can be displayed. A sample frame acquired using this approach is shown in Fig. 5.

As coupled-quantum-dot systems continue to scale in complexity, it will become increasingly important to rapidly obtain charge-stability diagrams and optimize the relevant tunneling rates. Traditionally, gate voltages have been optimized through a slow iterative process that involves changing gate voltages and observing the resulting charge-stability diagram. The process is time consuming, in

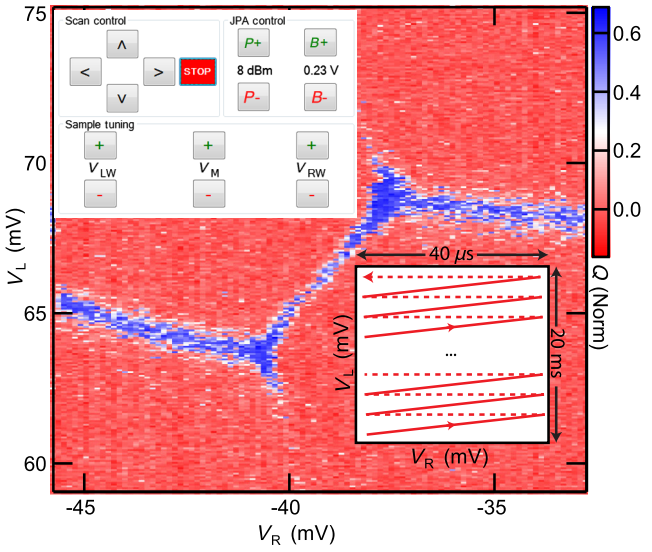

FIG. 5. Normalized Q quadrature amplitude as a function of V_{L} and V_{R}. The scan is acquired by rastering the gate voltages over a 20-ms period. The rastering scheme is illustrated in the lower inset. Starting in the lower left-hand corner of the stability diagram, V_{R} is repeatedly ramped with a 40-μs period. At the same time, V_{L} is ramped up with a 20-ms period. The rastering configuration is similar to cathode-ray-tube monitors. The high SNR then allows for real-time tuning of the DQD, which is accomplished using an intuitive user interface pictured in the upper inset.

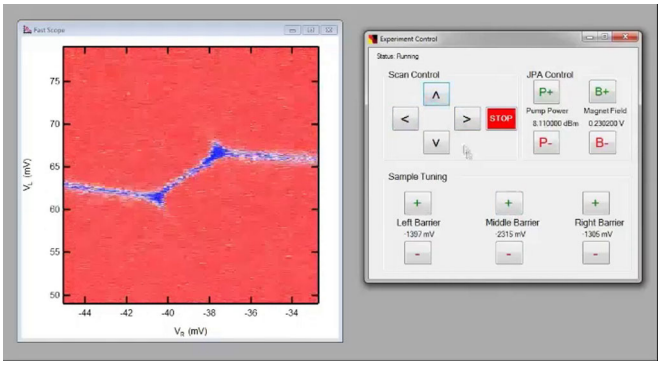

VIDEO 1. Demonstration of live tuning of a DQD device. We adjust the gate-voltage settings while the DQD charge-stability diagram is continuously acquired and displayed. Starting from a DQD, we first lower the left barrier until a single dot is formed. We then raise the left barrier to recover a DQD charge-stability diagram.

part due to the time necessary to acquire a new scan of the charge transition being tuned (often on the order of minutes). We build a simple user interface to control the experiment (see upper inset of Fig. 5) and use our rastering scheme to continuously update the charge transition in question. A set of buttons is used to interactively adjust electrostatic gate voltages, while the results of the parameter tuning are displayed in real time. This gives immediate feedback and allows one to arrive at the optimal gate voltages with ease. Video 1 is a demonstration of this form of device tuning.

V. CONCLUSION AND OUTLOOK

In conclusion, we use a JPA for fast measurements of a cavity-coupled semiconductor DQD. The addition of the JPA results in a factor of 2000 improvement in the SNR compared to the setup with the JPA turned off. As a result, the minimum time to detect a single charge is limited by the linewidth of the cavity. We also develop a dual gate-voltage rastering scheme that allows us to capture a charge-stability diagram in 20 ms. This technique enables real-time device tuning, which has the potential to greatly increase the rate at which complex quantum-dot devices are optimized.

The SNR enhancements also have important implications for readout of spin qubits. For a cavity-coupled DQD, the interdot charge transition signal is spin sensitive [41,52]. Because of the Pauli exclusion principle, spin singlet and triplet states have different charge susceptibilities. As a result, improvements in charge sensing directly translate into improvements in spin-state readout. Finally, the three layers of magnetic shielding that we employ allows integration of the JPA amplifier with spin qubit experiments, where magnetic fields are needed to Zeeman split the spin states [51]. It is, therefore, now feasible to take advantage of the highly desirable low-noise performance of superconducting amplifiers in spin qubit experiments.

ACKNOWLEDGMENTS

We thank Thomas Hazard, John Martinis, Josh Mutus, and Ted White for helpful discussions and Drew Baden for assistance with FPGA programming. Research is supported by the Packard Foundation, ARO Grant No. W911NF-15-1-0149, DARPA QuEST Grant No. HR0011-09-1-0007, and the NSF (Grants No. DMR-1409556 and DMR-1420541).

APPENDIX A: COMPLETE CIRCUIT DIAGRAM

The complete circuit diagram is shown in Fig. 6. The experiment consists of several subcomponents, which we now describe in detail:

(a) Gate-voltage generation circuit, which creates the appropriate time-dependent gate signals
(b) JPA pump and bias setup
(c) Demodulation circuit, which recovers the resultant I and Q quadratures

1. Gate-voltage generation

To generate the necessary time-dependent gate voltages, we employ three different instruments. First, a digital-to-analog converter (DAC) generates all of the dc gate voltages. The DAC outputs are filtered using a standard RC filter at room temperature and a combination of RC filters and Mini-Circuits LFCN-80 filters at the mixing chamber. For fast sweeping of gate voltages, ac signals are added to these dc gate biases. For sweeps of the left gate voltage V_L, we add the dc gate voltage generated by the DAC to the output of an Agilent 33522A waveform generator using a 10-μF capacitor. For sweeps of the right gate voltage V_R, the dc gate voltage is added to the output of a Tektronix AWG7000 using a bias tee formed from a 5.6-nF capacitor and 2.8-kΩ resistor. The bias tee is thermalized at the mixing chamber.

For the dual gate-voltage rastering in video mode, the AWG7000 generates the 40-μs V_R ramp, while the 33522A generates the 20-ms V_L ramp. We note that the cryogenic circuit is built symmetrically, which allows the rastering direction to be changed by simple switching of room-temperature cables. Finally, the marker output of the AWG7000 is used to synchronize the AWG7000 and the 33522A. Data acquisition is triggered using the sync output of the 33522A signal generator.

2. JPA pump tone and bias setup

The parametric amplifier is pumped by a tone f_{pump} using an Agilent 8257D signal generator. For JPA calibration, a room-temperature switch is used to divert the f_{in} tone into the pump port. The pump tone is added to the signal exiting the microwave cavity using a Krytar 120420 directional coupler. A second Krytar 120420 directional coupler can optionally be used to remove the pump tone (leaving just the amplified signal), by adding an appropriate

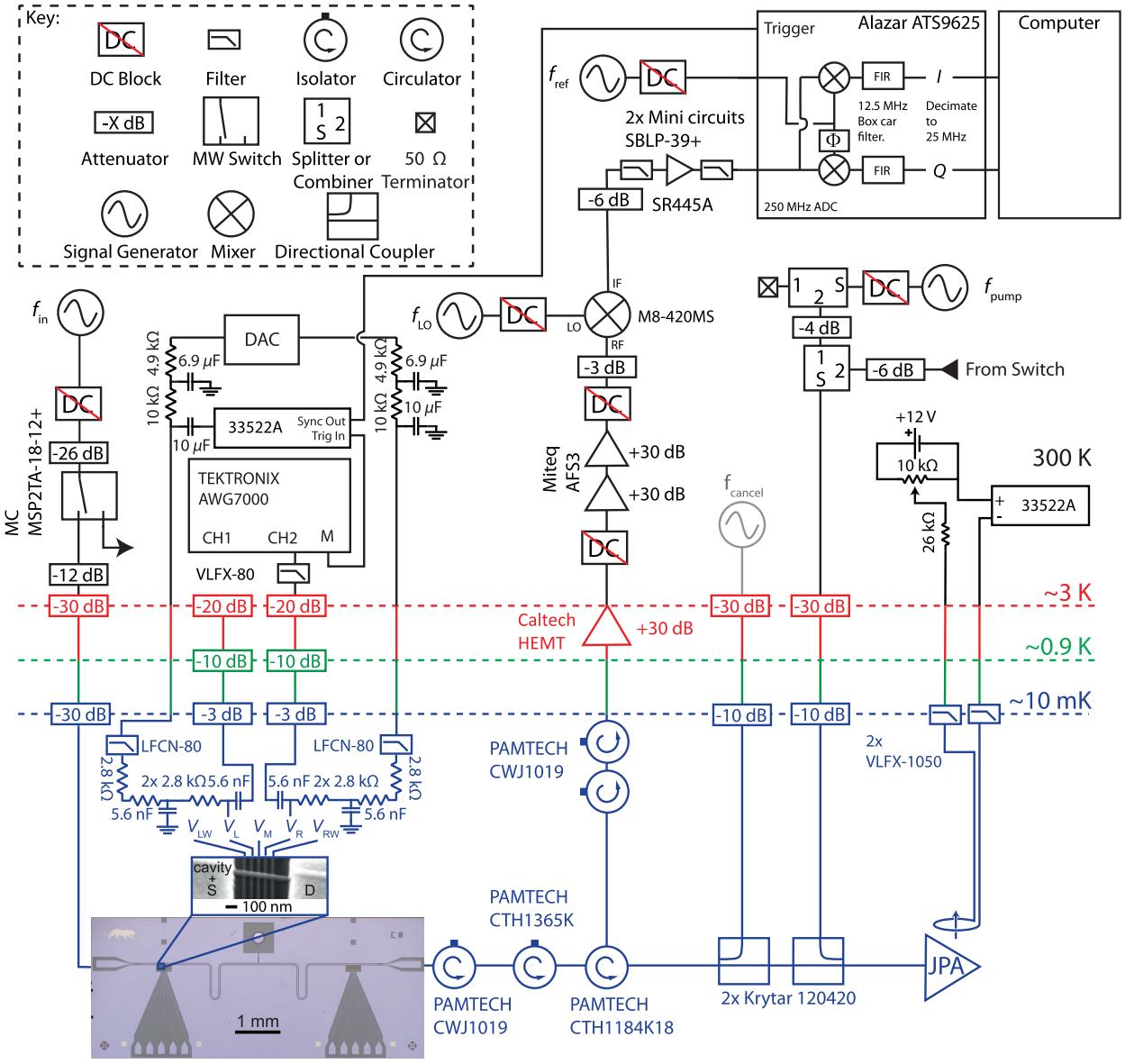

FIG. 6. Complete circuit diagram. All microwave sources and the Alazar data acquisition card are phase locked using a SRS FS725 frequency standard. The gray-colored components are not used in the present experiment.

cancellation tone with frequency f_{cancel}. However, it is not used in this experiment. The signal reflected off of the JPA is amplified using a high-electron-mobility transistor (HEMT) amplifier mounted to the 3-K plate of the dilution refrigerator. Two room-temperature Miteq AFS3 amplifiers provide additional signal amplification.

Two Pamtech isolators prevent the pump tone from leaking back towards the cavity, while an additional pair of isolators is used to prevent HEMT amplifier noise from traveling to the JPA. Finally, the dc magnetic field used to bias the JPA is generated by a small 6000 turn coil of superconducting wire. The coil is biased by adding a dc voltage generated by a battery to the output of an Agilent 33522A signal generator and allows very fine stepping of the magnetic field.

3. Heterodyne demodulation circuit

Frequency down-conversion to 12.5 MHz is achieved using a local oscillator (LO) tone f_{LO} and a Marki Microwave M8-420MS mixer. The signal is then filtered and further amplified before being digitized at 250 MHz by an Alazar ATS9625 FPGA-digitizer board. A reference 12.5-MHz signal is generated and digitized separately. The FPGA multiplies the two signals together generating the I quadrature signal. Additionally, the FPGA phase shifts the reference by 90° and multiplies it with the signal to generate the Q quadrature signal. Both I and Q signals are then filtered using a 12.5-MHz box-car filter to remove the 25-MHz image of the signal. The data stream is then passed to the computer over a PCI express bus.

APPENDIX B: EXTRACTION OF THE SIGNAL-TO-NOISE RATIO AS A FUNCTION OF τ

To extract the SNR [53] as a function of τ [see Fig. 4(e)], we first oversample at 12.5×10^6 samples/s. After the data are processed by the FPGA, we apply an additional filter:

$$Q_{\text{filter}}(t,\tau) = \frac{t_{\text{sample}}}{\tau} \sum_{t'=t-\tau/2}^{t+\tau/2} Q(t'). \tag{B1}$$

Here, the sum is taken over the discrete time steps spaced by $t_{\text{sample}} = 80$ ns, τ is the target integration time, t is time, and $Q(t)$ is the measured response. Equation (B1) is equivalent to a digital box-car filter and has an approximately $S(f) = \text{sinc}(f\tau)^2$ spectral response. Here, $\text{sinc}(x) = \sin(\pi x)/\pi x$ is the normalized sinc function, and f is the frequency. The spectral response is only approximate due to finite digitizer resolution and discrete sampling.

For large τ, the above technique becomes impractical due to the exceedingly slow gate-voltage sweeps (compared to the frequency response of the voltage adders) and the large amounts of data that are generated. To access longer values of τ, we instead repeatedly sweep through the charge transition of interest with a 50-Hz repetition rate. Multiple time traces are averaged to obtain a longer effective integration time τ:

$$Q_{\text{av}}(t,\tau) = \sum_{k=1}^{\tau/12.5\ \mu\text{s}} \frac{Q_{\text{filter}}(t + (k-1) \times 20\ \text{ms}, 12.5\ \mu\text{s})}{\tau/12.5\ \mu\text{s}}. \tag{B2}$$

[1] J. Bylander, T. Duty, and P. Delsing, Current measurement by real-time counting of single electrons, Nature (London) **434**, 361 (2005).

[2] M. A. Topinka, B. J. LeRoy, S. E. J. Shaw, E. J. Heller, R. M. Westervelt, K. D. Maranowski, and A. C. Gossard, Imaging coherent electron flow from a quantum point contact, Science **289**, 2323 (2000).

[3] J. Martin, N. Akerman, G. Ulbricht, T. Lohmann, J. H. Smet, K. von Klitzing, and A. Yacoby, Observation of electron-hole puddles in graphene using a scanning single-electron transistor, Nat. Phys. **4**, 144 (2008).

[4] R. C. Ashoori, H. L. Stormer, J. S. Weiner, L. N. Pfeiffer, S. J. Pearton, K. W. Baldwin, and K. W. West, Single-Electron Capacitance Spectroscopy of Discrete Quantum Levels, Phys. Rev. Lett. **68**, 3088 (1992).

[5] O. E. Dial, R. C. Ashoori, L. N. Pfeiffer, and K. W. West, High-resolution spectroscopy of two-dimensional electron systems, Nature (London) **448**, 176 (2007).

[6] R. Hanson, L. P. Kouwenhoven, J. R. Petta, S. Tarucha, and L. M. K. Vandersypen, Spins in few-electron quantum dots, Rev. Mod. Phys. **79**, 1217 (2007).

[7] W. G. van der Wiel, S. De Franceschi, J. M. Elzerman, T. Fujisawa, S. Tarucha, and L. P. Kouwenhoven, Electron transport through double quantum dots, Rev. Mod. Phys. **75**, 1 (2002).

[8] K. Ono, D. G. Austing, Y. Tokura, and S. Tarucha, Current rectification by Pauli exclusion in a weakly coupled double quantum dot system, Science **297**, 1313 (2002).

[9] A. C. Johnson, J. R. Petta, C. M. Marcus, M. P. Hanson, and A. C. Gossard, Singlet-triplet spin blockade and charge sensing in a few-electron double quantum dot, Phys. Rev. B **72**, 165308 (2005).

[10] M. Field, C. G. Smith, M. Pepper, D. A. Ritchie, J. E. F. Frost, G. A. C. Jones, and D. G. Hasko, Measurements of Coulomb Blockade with a Noninvasive Voltage Probe, Phys. Rev. Lett. **70**, 1311 (1993).

[11] M. H. Devoret and R. J. Schoelkopf, Amplifying quantum signals with the single-electron transistor, Nature (London) **406**, 1039 (2000).

[12] W. Lu, Z. Ji, L. Pfeiffer, K. W. West, and A. J. Rimberg, Real-time detection of electron tunnelling in a quantum dot, Nature (London) **423**, 422 (2003).

[13] R. J. Schoelkopf, P. Wahlgren, A. A. Kozhevnikov, P. Delsing, and D. E. Prober, The radio-frequency single-electron transistor (RF-SET): A fast and ultrasensitive electrometer, Science **280**, 1238 (1998).

[14] A. Cottet, C. Mora, and T. Kontos, Mesoscopic admittance of a double quantum dot, Phys. Rev. B **83**, 121311 (2011).

[15] K. D. Petersson, C. G. Smith, D. Anderson, P. Atkinson, G. A. C. Jones, and D. A. Ritchie, Charge and spin state readout of a double quantum dot coupled to a resonator, Nano Lett. **10**, 2789 (2010).

[16] S. Weinreb, J. Bardin, H. Mani, and G. Jones, Matched wideband low-noise amplifiers for radio astronomy, Rev. Sci. Instrum. **80**, 044702 (2009).

[17] C. Barthel, D. J. Reilly, C. M. Marcus, M. P. Hanson, and A. C. Gossard, Rapid Single-Shot Measurement of a Singlet-Triplet Qubit, Phys. Rev. Lett. **103**, 160503 (2009).

[18] C. Barthel, M. Kjærgaard, J. Medford, M. Stopa, C. M. Marcus, M. P. Hanson, and A. C. Gossard, Fast sensing of double-dot charge arrangement and spin state with a radio-frequency sensor quantum dot, Phys. Rev. B **81**, 161308 (2010).

[19] J. I. Colless, A. C. Mahoney, J. M. Hornibrook, A. C. Doherty, H. Lu, A. C. Gossard, and D. J. Reilly, Dispersive Readout of a Few-Electron Double Quantum Dot with Fast rf Gate Sensors, Phys. Rev. Lett. **110**, 046805 (2013).

[20] E. A. Tholén, A. Ergl, E. M. Doherty, F. M. Weber, F. Grgis, and D. B. Haviland, Nonlinearities and parametric amplification in superconducting coplanar waveguide resonators, Appl. Phys. Lett. **90**, 253509 (2007).

[21] T. Yamamoto, K. Inomata, M. Watanabe, K. Matsuba, T. Miyazaki, W. D. Oliver, Y. Nakamura, and J. S. Tsai, Flux-driven Josephson parametric amplifier, Appl. Phys. Lett. **93**, 042510 (2008).

[22] M. A. Castellanos-Beltran, K. D. Irwin, G. C. Hilton, L. R. Vale, and K. W. Lehnert, Amplification and squeezing of

quantum noise with a tunable Josephson metamaterial, Nat. Phys. **4**, 929 (2008).
[23] R. Vijay, M. H. Devoret, and I. Siddiqi, The Josephson bifurcation amplifier, Rev. Sci. Instrum. **80**, 111101 (2009).
[24] N. Bergeal, F. Schackert, M. Metcalfe, R. Vijay, V. E. Manucharyan, L. Frunzio, D. E. Prober, R. J. Schoelkopf, S. M. Girvin, and M. H. Devoret, Phase-preserving amplification near the quantum limit with a Josephson ring modulator, Nature (London) **465**, 64 (2010).
[25] B. Ho Eom, P. K. Day, H. G. LeDuc, and J. Zmuidzinas, A wideband, low-noise superconducting amplifier with high dynamic range, Nat. Phys. **8**, 623 (2012).
[26] B. Abdo, K. Sliwa, L. Frunzio, and M. Devoret, Directional Amplification with a Josephson Circuit, Phys. Rev. X **3**, 031001 (2013).
[27] C. Caves, Quantum limits on noise in linear amplifiers, Phys. Rev. D **26**, 1817 (1982).
[28] C. M. Caves, J. Combes, Z. Jiang, and S. Pandey, Quantum limits on phase-preserving linear amplifiers, Phys. Rev. A **86**, 063802 (2012).
[29] R. Vijay, D. H. Slichter, and I. Siddiqi, Observation of Quantum Jumps in a Superconducting Artificial Atom, Phys. Rev. Lett. **106**, 110502 (2011).
[30] Y. Chen, D. Sank, P. O'Malley, T. White, R. Barends, B. Chiaro, J. Kelly, E. Lucero, M. Mariantoni, A. Megrant *et al.*, Multiplexed dispersive readout of superconducting phase qubits, Appl. Phys. Lett. **101**, 182601 (2012).
[31] R. Vijay, C. Macklin, D. H. Slichter, S. J. Weber, K. W. Murch, R. Naik, A. N. Korotkov, and I. Siddiqi, Stabilizing Rabi oscillations in a superconducting qubit using quantum feedback, Nature (London) **490**, 77 (2012).
[32] P. Campagne-Ibarcq, E. Flurin, N. Roch, D. Darson, P. Morfin, M. Mirrahimi, M. H. Devoret, F. Mallet, and B. Huard, Persistent Control of a Superconducting Qubit by Stroboscopic Measurement Feedback, Phys. Rev. X **3**, 021008 (2013).
[33] J. D. Teufel, T. Donner, D. Li, J. W. Harlow, M. S. Allman, K. Cicak, A. J. Sirois, J. D. Whittaker, K. W. Lehnert, and R. W. Simmonds, Sideband cooling of micromechanical motion to the quantum ground state, Nature (London) **475**, 359 (2011).
[34] C. Eichler, C. Lang, J. M. Fink, J. Govenius, S. Filipp, and A. Wallraff, Observation of Entanglement between Itinerant Microwave Photons and a Superconducting Qubit, Phys. Rev. Lett. **109**, 240501 (2012).
[35] R. Movshovich, B. Yurke, P. G. Kaminsky, A. D. Smith, A. H. Silver, R. W. Simon, and M. V. Schneider, Observation of Zero-Point Noise Squeezing via a Josephson-Parametric Amplifier, Phys. Rev. Lett. **65**, 1419 (1990).
[36] C. Eichler, D. Bozyigit, C. Lang, M. Baur, L. Steffen, J. M. Fink, S. Filipp, and A. Wallraff, Observation of Two-Mode Squeezing in the Microwave Frequency Domain, Phys. Rev. Lett. **107**, 113601 (2011).
[37] L. Gaudreau, S. A. Studenikin, A. S. Sachrajda, P. Zawadzki, A. Kam, J. Lapointe, M. Korkusinski, and P. Hawrylak, Stability Diagram of a Few-Electron Triple Dot, Phys. Rev. Lett. **97**, 036807 (2006).
[38] T. Takakura, A. Noiri, T. Obata, T. Otsuka, J. Yoneda, K. Yoshida, and S. Tarucha, Single to quadruple quantum dots with tunable tunnel couplings, Appl. Phys. Lett. **104**, 113109 (2014).
[39] D. D. Awschalom, L. C. Bassett, A. S. Dzurak, E. L. Hu, and J. R. Petta, Quantum spintronics: Engineering and manipulating atom-like spins in semiconductors, Science **339**, 1174 (2013).
[40] T. Frey, P. J. Leek, M. Beck, A. Blais, T. Ihn, K. Ensslin, and A. Wallraff, Dipole Coupling of a Double Quantum Dot to a Microwave Resonator, Phys. Rev. Lett. **108**, 046807 (2012).
[41] K. D. Petersson, L. W. McFaul, M. D. Schroer, M. Jung, J. M. Taylor, A. A. Houck, and J. R. Petta, Circuit quantum electrodynamics with a spin qubit, Nature (London) **490**, 380 (2012).
[42] M. R. Delbecq, V. Schmitt, F. D. Parmentier, N. Roch, J. J. Viennot, G. Fève, B. Huard, C. Mora, A. Cottet, and T. Kontos, Coupling a Quantum Dot, Fermionic Leads, and a Microwave Cavity on a Chip, Phys. Rev. Lett. **107**, 256804 (2011).
[43] S. Nadj-Perge, S. M. Frolov, E. P. A. M. Bakkers, and L. P. Kouwenhoven, Spin-orbit qubit in a semiconductor nanowire, Nature (London) **468**, 1084 (2010).
[44] M. D. Schroer and J. R. Petta, Correlating the nanostructure and electronic properties of InAs nanowires, Nano Lett. **10**, 1618 (2010).
[45] C. Fasth, A. Fuhrer, L. Samuelson, V. N. Golovach, and D. Loss, Direct Measurement of the Spin-Orbit Interaction in a Two-Electron InAs Nanowire Quantum Dot, Phys. Rev. Lett. **98**, 266801 (2007).
[46] D. B. Suyatin, C. Thelander, M. T. Björk, I. Maximov, and L. Samuelson, Sulfur passivation for ohmic contact formation to InAs nanowires, Nanotechnology **18**, 105307 (2007).
[47] G. J. Dolan, Offset masks for lift-off processing, Appl. Phys. Lett. **31**, 337 (1977).
[48] C. Eichler and A. Wallraff, Controlling the dynamic range of a Josephson parametric amplifier, EPJ Quantum Technol. **1**, 2 (2014).
[49] D. Ristè, J. G. van Leeuwen, H.-S. Ku, K. W. Lehnert, and L. DiCarlo, Initialization by Measurement of a Superconducting Quantum Bit Circuit, Phys. Rev. Lett. **109**, 050507 (2012).
[50] M. Jung, M. D. Schroer, K. D. Petersson, and J. R. Petta, Radio frequency charge sensing in InAs nanowire double quantum dots, Appl. Phys. Lett. **100**, 253508 (2012).
[51] J. R. Petta, A. C. Johnson, J. M. Taylor, E. A. Laird, A. Yacoby, M. D. Lukin, C. M. Marcus, M. P. Hanson, and A. C. Gossard, Coherent manipulation of coupled electron spins in semiconductor quantum dots, Science **309**, 2180 (2005).
[52] M. D. Schroer, M. Jung, K. D. Petersson, and J. R. Petta, Radio Frequency Charge Parity Meter, Phys. Rev. Lett. **109**, 166804 (2012).
[53] P. Horowitz and W. Hill, *Art of Electronics* (Cambridge University Press, New York, 1989), Chap. 7, pp. 391–470.
[54] A. Aassime, G. Johansson, G. Wendin, R. J. Schoelkopf, and P. Delsing, Radio-Frequency Single-Electron Transistor as Readout Device for Qubits: Charge Sensitivity and Backaction, Phys. Rev. Lett. **86**, 3376 (2001).

[55] J. Y. Mutus, T. C. White, R. Barends, Y. Chen, Z. Chen, B. Chiaro, A. Dunsworth, E. Jeffrey, J. Kelly, A. Megrant *et al.*, Strong environmental coupling in a Josephson parametric amplifier, Appl. Phys. Lett. **104**, 263513 (2014).

[56] C. Eichler, Y. Salathe, J. Mlynek, S. Schmidt, and A. Wallraff, Quantum-Limited Amplification and Entanglement in Coupled Nonlinear Resonators, Phys. Rev. Lett. **113**, 110502 (2014).

[57] K. O'Brien, C. Macklin, I. Siddiqi, and X. Zhang, Resonant Phase Matching of Josephson Junction Traveling Wave Parametric Amplifiers, Phys. Rev. Lett. **113**, 157001 (2014).

[58] T. White, J. Mutus, I.-C. Hoi, B. Barends, R. Campbell, Y. Chen, Z. Chen, B. Chiaro, A. Dunsworth, E. Jeffrey *et al.*, Traveling wave parametric amplifier with Josephson junctions using minimal resonator phase matching, arXiv: 1503.04364.